ADVANCED HEALTHCARE MATERIALS
www.advhealthmat.de

Stretchable Optomechanical Fiber Sensors for Pressure Determination in Compressive Medical Textiles

*Joseph D. Sandt, Marie Moudio, J. Kenji Clark, James Hardin, Christian Argenti, Matthew Carty, Jennifer A. Lewis, and Mathias Kolle**

Medical textiles are widely used to exert pressure on human tissues during treatment of post-surgical hematoma, burn-related wounds, chronic venous ulceration, and other maladies. However, the inability to dynamically sense and adjust the applied pressure often leads to suboptimal pressure application, prolonging treatment or resulting in poor patient outcomes. Here, a simple strategy for measuring sub-bandage pressure by integrating stretchable optomechanical fibers into elastic bandages is demonstrated. Specifically, these fibers possess an elastomeric photonic multilayer cladding that surrounds an extruded stretchable core filament. They can sustain repetitive strains of over 100%, and respond to deformation with a predictable and reversible color variation. Integrated into elastic textiles, which apply pressure as a function of their strain, these fibers can provide instantaneous and localized pressure feedback. These colorimetric fiber sensors are well suited for medical textiles, athletic apparel, and other smart wearable technologies, especially when repetitive, large deformations are required.

Engineered medical textiles[1,2] are widely employed in compression therapy, in which a well-controlled pressure gradient is applied to a patient's limb or other body part. This approach is used to treat a broad array of medical conditions, including post-surgical hematoma, burn-related wounds, lymphedema, scarring, and chronic venous ulceration.[3] Optimal pressure ranges that promote healing have been estimated to vary between 30 and 50 mmHg gauge pressure (i.e., 4.0–6.7 kPa),[4] but the correct "dosage" for compression therapy varies between patients based on their body structure and medical condition.[5] Beyond this relatively narrow pressure range, compression therapy becomes ineffective and could potentially result in further injury to the patient.[5–7] Over one percent of all people in industrialized countries suffer from venous leg ulcers,[8] which are typically treated by compression therapy. For over 600 000 patients in the United States alone, ineffective treatment leads to the loss of around two million work days and unnecessary additional health-care costs of up to five billion dollars each year.[9,10] Chronic venous ulceration is increasingly prevalent in persons over 65 years of age, and with a growing and aging world population, there is a pressing need to improve compression treatment.[9,10]

While the design and mechanics of compressive medical textiles have improved,[11] they still do not provide quantitative, localized feedback regarding the pressure exerted by a bandage on a patient's body.[4,6] One common strategy is to limit the maximal pressure that a textile can exert on an underlying limb.[3] However, these pressure-limiting textiles are difficult to manipulate at high strains, and cannot be adjusted to suit individual patients. While thin sensors can be placed under bandages or directly onto a patient's skin to determine the applied pressure,[12,13] they can only provide information for particular regions of a treated area, and may themselves affect the pressure being applied. Moreover, if the sensors are removed, they cannot provide pressure information throughout bandage use.

Here, we demonstrate a method for quantifying sub-bandage pressure using stretchable optomechanical fibers as colorimetric strain sensors (**Figure 1**a). Specifically, we design, manufacture, and characterize photonic fibers with a highly elastic, periodic multilayer cladding that gives rise to coupled optical and mechanical properties.[14] The cladding is composed of alternating thin layers of transparent polydimethylsiloxane (PDMS, refractive index $n \approx 1.41$) and a polystyrene-polyisoprene triblock copolymer (PSPI, $n \approx 1.55$) (Figure 1b). This

J. D. Sandt, M. Moudio, C. Argenti, Prof. M. Kolle
Mechanical Engineering Department
Massachusetts Institute of Technology
Cambridge, MA 02139, USA
E-mail: mkolle@mit.edu
J. K. Clark
Department of Mechanical Engineering
The University of Tokyo
Tokyo 113-8654, Japan
Dr. J. Hardin
United States Air Force Research Lab
Wright-Patterson Air Force Base
Wright-Patterson AFB
OH 45433, USA
Prof. M. Carty
Center for Surgery and Public Health
Brigham and Women's Hospital-Harvard Medical School
Boston, MA 02115, USA
Prof. J. A. Lewis
John A. Paulson School of Engineering and Applied Science
Harvard University
Cambridge, MA 02138, USA
The ORCID identification number(s) for the author(s) of this article can be found under https://doi.org/10.1002/adhm.201800293.

DOI: 10.1002/adhm.201800293

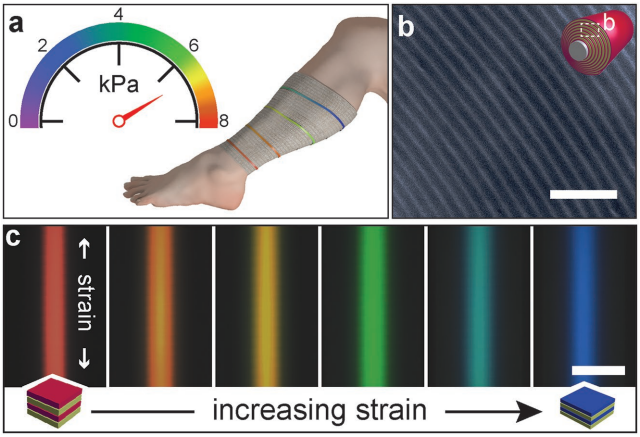

Figure 1. Concept for sensing bandage pressure. a) Depiction of the proposed use of fibers as colorimetric sub-bandage pressure indicators in compression therapy. b) Scanning electron microscopy image of a cross-section of a multilayer cladding, showing its distinct radial periodicity. Scale bar 2 µm. c) A series of optical micrographs showing the vivid, strain-dependent color of a fiber that is colored red when no strain is applied and changes to orange, yellow, green, and finally blue as the strain increases and the layer period decreases. The direction of applied strain is marked in the first image. Scale bar 100 µm. The color sequence is reversed from the conceptual sketch in (a), which will be addressed in the Discussion section.

layered architecture acts as a Bragg reflector that strongly reflects visible light in a narrow spectral range. Importantly, these materials form transparent thin films that exhibit an elastic response up to at least 350% elongation;[15] furthermore, their refractive index contrast is sufficiently small to avoid overly broad reflection bands that would compromise color purity and strain sensitivity. The two constituent materials also possess similar Poisson's ratios, which reduces the chance that cladding layers will separate from either themselves or the fiber core during elongation.

The nanoscale periodicity of the alternating thin films within the multilayer cladding determines the location of the fibers' reflection band in the visible light spectrum. The central wavelength of a fiber's reflection band λ_C is a function of the applied axial true strain ε, the fiber's Poisson's ratio ν, and the central wavelength λ_0 of the stop band at zero strain, as given by Equation (1) (see the Supporting Information for a full derivation)

$$\lambda_C = \lambda_0 \, e^{-\nu\varepsilon} \tag{1}$$

The color of a fiber at zero strain, and thus its strain-dependent colors, can be adjusted by controlling the periodicity of the multilayer cladding during manufacturing. When a fiber's diameter and cladding layer period change upon stretching and relaxation, a reversible color change is observed that can traverse the entire visible range (Figure 1c). This interdependence between an applied load, its corresponding strain, and the observed color change can be harnessed in integrated fiber-based sensors that provide real-time feedback for applied pressure in compression therapy, since the pressure exerted by an elastic bandage on a patient's body is related to the strain in that bandage.[6] By directly monitoring the reversible color shift of these optomechanical fibers integrated into compressive medical textiles, we demonstrate a method for quickly, locally, and accurately quantifying sub-bandage pressure in multiple localized regions of interest.

We fabricate stretchable colorimetric fiber sensors by wrapping a thin bilayer of PDMS and PSPI (100–300 nm layers) 30–60 times around an extruded PDMS core filament (**Figure 2**a–c). The core filament is rendered light-absorbing by adding a black dye prior to extrusion, which attenuates light in the spectral range transmitted by the cladding to ensure that its bright reflection colors are not obscured (Figure 2b, bottom right). By separately manufacturing and subsequently assembling the fiber core and cladding, we independently control the structure of each component. For example, the thicknesses of the individual layers within the cladding can be controlled by varying the polymer concentration in solution and the spinning speed used in the coating process (Figure 2a, bottom). The thickness of these cladding layers dictates the fiber cladding's zero-strain color and the range of colors observed as they are strained. The core filaments can be fabricated so that their geometric, optical, and mechanical properties vary along their length (Figure 2b, bottom left). It is therefore possible to create fiber sensors that exhibit varying sensitivity to applied forces along their length, enhance or counteract the angular dependency of observed color, or transmit or absorb light not reflected by the cladding. During fiber assembly (Figure 2c), the rolling process can be modified to form multilayer claddings with multiple distinct periodicities, chirped layered architectures, and other engineered cladding designs, which lead to more complex spectral landscapes of light reflected by these fibers (Figure 2d). Representative fibers with distinct coloration obtained by varying the aforementioned parameters in cladding and core design are highlighted in Figure 2e. Moreover, a wide range of elastomeric and stimuli-responsive materials could be assembled into multilayer architectures by this approach.

To quantitatively assess the fibers' optomechanical performance, we subjected them to many cycles of stretching and relaxation. Using a custom-made optical setup, we simultaneously measured the fibers' stress–strain behavior, reflection spectra, and microscale optical appearance over a wide range of controlled deformations to determine whether their vivid, colorimetric response is altered or diminished with repeated exposure to large strains (see the Experimental Section for more details). Specifically, the fibers are subjected to 10 000 cycles of stretching up to 0.75 true strain (which corresponds to 1.12 engineering strain, i.e., an elongation of the fibers to over twice their original length). Data collected during cycles 1, 10, 100, 1000, and 10 000 are shown in **Figure 3**a,b. These tests reveal that the fibers' optical and mechanical response to strain is both remarkably consistent and robust. Importantly, the spectral position of the fibers' reflection peak at each strain is consistent between cycles: the central wavelength of reflection peaks for arbitrary levels of strain shift by less than 3 nm on average, and no more than 5 nm, over 10 000 cycles (Figure 3c). Converting the measured spectra to points on the International Commission on Illumination (CIE) x-y chromaticity diagram[16] (a common way of representing the gamut of hues perceivable with the human eye) further demonstrates the consistency of reflected colors over cyclic stretching, with points at comparable levels of strain from different cycles clustering closely together

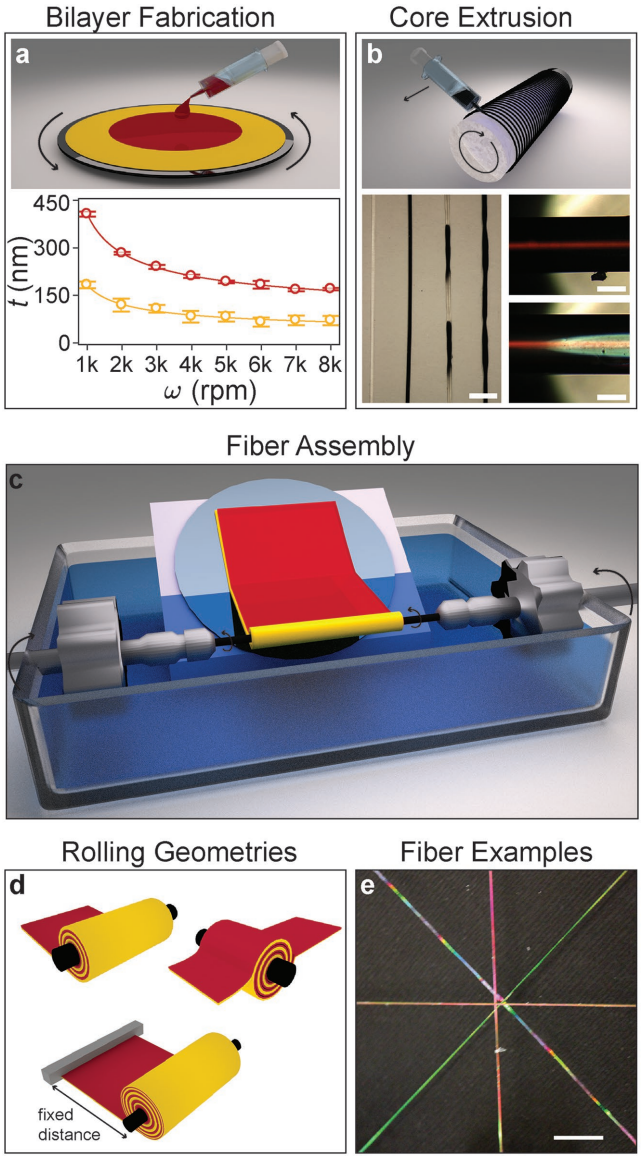

Figure 2. Modular fiber manufacture. a) Depiction of the spin coating process, and a graph showing how the spin speed ω affects the film thicknesses t in the fiber cladding bilayer (red: PSPI layer; yellow: PDMS layer for solution concentrations of 4% by weight). Mean and standard deviation are plotted from $n = 4$ data points for each solution at each spin speed. b) Depiction of the fiber core extrusion process, images of extruded fiber cores (lower left, note how thickness and opacity are controllably varied in the rightmost two samples; scale bar 2 mm), and two images (lower right; scale bars 100 µm) showing how absorbing cores preserve color in reflection (top) by eliminating light that is transmitted through the cladding and would pass through a transparent core (bottom). c) Depiction of the fiber rolling process, in which a spin-coated bilayer is wrapped around an elastomeric core fiber to form the multilayer cladding. d) Schematics of different rolling geometries. Clockwise from top left are shown rolling from a free end of the bilayer to generate fibers with one periodicity, rolling from an axis between a free end and the midpoint of a bilayer to create fibers with two regions of periodicity, and rolling from the free end of a bilayer with the opposite end fixed for chirped multilayer claddings. e) A photograph of several fibers; the rainbow-colored fiber periodically varies in thickness along its length, leading to a varying strain and coloration (scale bar 1 mm).

(Figure 3d). After 10 000 cycles, the fibers' average reflection strength diminished from 86% to 73%, a relative drop of about 15%, which initiates only after more than 1000 stretch cycles (Figure 3e). Nonetheless, even after 10 000 cycles, the fibers are highly visible and appear brighter than conventional means of textile coloration, such as pigments or dyes.

For the sensing applications of interest, each fiber should ideally reflect the same color from any point along its length. To assess their color consistency, both spectra and microscopy images are recorded along the length of several fibers at prescribed strains (see the Experimental Section for further details). While well-manufactured fibers exhibited homogenous coloration along their lengths (**Figure 4**a), we did find that defects introduced via the spin coating or fiber rolling processes reduced color uniformity (Figure 4b). Yet even defective fibers exhibited well-defined color trajectories as a function of strain (Figure 4d, in which the fiber transitions from blue to green via violet, red, orange, and yellow). The color variability along a given fiber at arbitrary strains is significantly lower for well-manufactured samples, as seen by comparing the standard deviations in Figure 4c,d.

Finally, we calculated the color trajectories of model fibers in the CIE color space to predict their color response and guide future assembly efforts. Figure 4e,f shows a selection of three simulated color trajectories and their corresponding spectra as a function of strain, respectively. Additional data comparing the predicted and experimentally measured colorimetric responses to strain are provided in Figure S4 (Supporting Information). Given our ability to control the cladding and core's composition and structure independently during manufacture, it is possible to design a wide variety of tailored color responses for specific strain levels.

To demonstrate pressure sensing during compression therapy, we integrated the stretchable, optomechanical fibers into bandage materials. As a simple proof-of-concept, we stitched the fibers onto single-component elastic compression bandages and validated their function as integrated sensors for sub-bandage pressure measurements using a custom-built apparatus. This apparatus allows an elastic bandage to be wrapped around a simulated leg at well-controlled strains. A compressible bladder is attached to a pressure gauge (see the Experimental Section and Figure S2 in the Supporting Information) to measure sub-bandage pressure, while an integrated camera and optical fiber spectrometer enable the collection of images and reflection spectra from the textile-integrated fiber sensors, in conjunction with the acquisition of strain and pressure data. Using this device, we first determined the relationship between bandage strain and sub-bandage pressure (**Figure 5**b), and then confirmed that a direct link between fiber color and sub-bandage pressure could be established in fiber-integrated bandages (Figure 5c). Importantly, these integrated fiber sensors retain their strong colorimetric response to applied strain when incorporated into compression bandages (Figure 5c, top inset images), and provide a clear colorimetric indication of the pressure beneath the bandage.

To assess the efficacy of bandages within integrated fiber sensors, we subjected a group of volunteers to compression therapy with varying target pressures applied to different locations on their legs using three different bandages: a plain

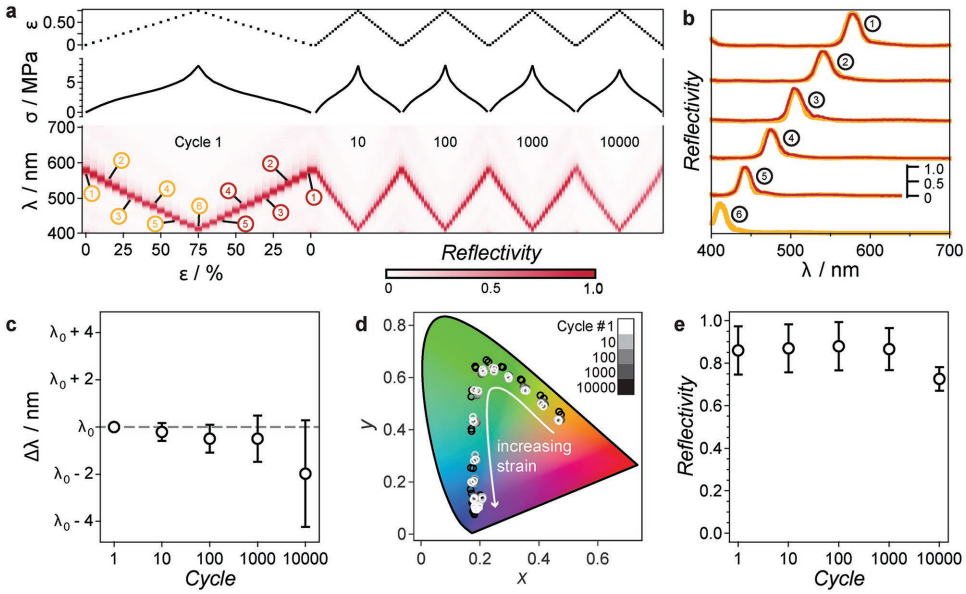

Figure 3. Cyclic fiber stretching. a) Stress, strain, and reflection spectra from one point on a fiber at cycles 1, 10, 100, 1000, and 10 000 of being stretched to 75% true strain and returned to a relaxed state. b) Reflection spectra at increasing (yellow) and decreasing (red) levels of strains during the first stretching cycle, marked with the same numbers as in (a). Spectra are offset from each other for clarity. c) Deviation from the initial central peak wavelength (the difference in central wavelength of peaks at cycle 1 and later cycles, averaged across all strain levels) over cycles. Mean and standard deviation are plotted, calculated from $n = 21$ different strain states in each analyzed stretch cycle. d) Fiber hue as a function of strain plotted in the CIE x-y color space. Fiber colors were obtained from spectra using the CIE 1931 2° Standard Observer color matching functions. The points show the fiber hue for increasing true strain from 0 to 0.75 in the cycles plotted above in (a). Points from different cycles for each level of strain are clustered tightly together in the CIE plot, providing further evidence for the high persistence of fiber color as a function of strain over cycles. e) Reflectivity of the fiber in each examined cycle. Mean and standard deviation are plotted, calculated from $n = 21$ points, as in (c). Points and spectra without error bars are representative samples. See the Experimental Section for more information.

bandage (unmarked, first control), a bandage with geometric markings that are supposed to indicate when a given target pressure is reached (second control), and a prototype bandage with integrated color-changing fibers. In the latter case, volunteers are provided with a color chart that relates the observed fiber color to the applied pressure (see Figure S3 in the Supporting Information). Using the same pressure measurement bladder described before, we determined the precision with which volunteers applied desired levels of pressure. The results indicate that each volunteer was able to apply pressures considerably closer to target values when using bandages with integrated fiber sensors (Figure 5d–f). For each target pressure, the measured pressures applied by different bandage systems are generally found to be statistically different (Figure 5e) ($p < 0.02$ for seven of nine comparisons; $p \approx 0.05$ for comparing pressures applied by the geometric bandage and fiber bandage on the mid-calf; $p < 0.10$ for comparing the plain bandage to the fiber bandage on the ankle). The bias, i.e., the difference of the means and the desired target pressures, is estimated for each bandage system and application location (Figure 5f). All biases for the plain bandage are significantly different than zero, while two of three biases for the bandage with geometric pressure indicators are significantly different than zero. However, none of the three biases for the bandages with integrated fiber sensors are significantly different than zero. Additionally, the distributions for pressures applied with fiber-integrated bandages had comparable, or smaller, standard deviations, than both control bandages tested. Hence, in practice, compression therapy administered using our fiber-sensor integrated bandages should yield more efficient and successful compression therapy treatment.

We have demonstrated the potential of stretchable optomechanical fiber sensors integrated into elastic medical textiles, such as bandages, to provide reliable, localized, and instantaneous determination of sub-bandage pressure applied during compression therapy. Thanks to the structure of their photonic cladding, the fibers respond to applied strain with a predictable, reversible, and easily observed color change that persists over several thousand cycles of deformation. This color shift is preserved upon integration of fibers into elastic textiles, allowing the observed fiber color to be correlated to the applied sub-bandage pressure.

Modular fabrication of these fibers enables us to control their composition, structure, and optomechanical properties. This manufacturing strategy could be used to produce similarly colorful fibers out of any two materials that are transparent, can be processed into thin films, and have sufficiently distinct refractive indices. Appropriate selection of the fibers' constituent materials could result in sensors that respond to thermal gradients, the presence of solvent vapors, stimulation by electromagnetic fields, and other phenomena with a predictable, observable change in their vivid coloration.[17–23]

The ability to fine-tune the film thicknesses in the fibers' multilayer claddings during manufacture is critical for designing fibers that display specific color variations in response to relevant levels of strain. While the physics underlying the fibers'

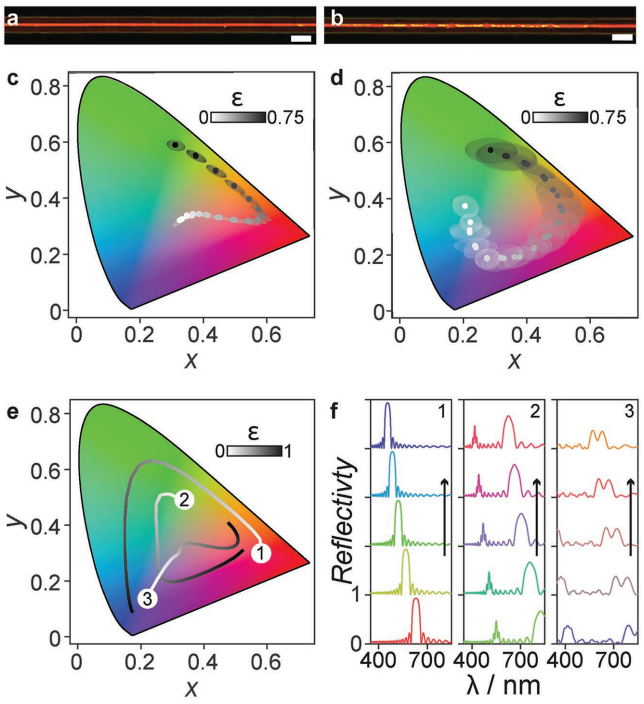

Figure 4. Color uniformity. a) Fiber with low defect density. b) Fiber with a higher defect density. Scale bars in (a) and (b) 100 µm. c) Color trajectory of a high-quality fiber in response to increasing strain levels. The arithmetic means of $n = 15$ points in CIE color space collected from varying fiber locations for each level of strain are plotted, with ovals representing standard deviations (from the same 15 points) in coordinate systems aligned to linear regressions of each cluster of colors. d) Color trajectory of a fiber with a high defect density. Arithmetic means and standard deviations are plotted as in (c), $n = 15$ points. Note how the fiber with markedly fewer defects [(a) and (c)] has considerably less variation in its microscopically observed color. e) Theoretical color trajectories for three fibers with different multilayer morphologies. f) Spectra of the three modeled fibers along their color trajectory for increasing strains.

color-changing mechanism prescribes a shift of the fibers' reflection peaks to lower wavelengths (a "blueshift") with increasing strain, it is possible to design fibers with multiple, carefully positioned reflection peaks, to create an apparent shift to red hues. Such fibers would appear to transition from a blue or green coloration to a red or orange hue at some prescribed strain, as predicted by the second and third CIE color space trajectories in Figure 4e. This could boost sensor utility by aligning the fibers' color trajectory with the human perception of signal colors by indicating dangerous levels of strain with bright red hues, as red stimuli have been shown to receive an attentional advantage.[24]

For this study, we tailored the fibers to appear yellow ($\lambda \simeq$ 580 nm) in the center of the target pressure range (40 mmHg, 5.33 kPa). The color yellow occupies the narrowest bandwidth of any color in the visible light spectrum, enabling greater sensitivity within and near the target pressure range (see fiber images in Figure 5c), thereby providing increased precision in bandage pressure control.

When used by untrained volunteers, bandages with integrated fiber sensors significantly enhanced the accuracy of the applied pressure relative to target pressures of interest, compared to commonly used, commercially available bandage systems. Our results indicate that the proposed integrated bandage pressure sensors could greatly improve the efficiency of compression therapy, leading to reduced treatment duration, improved patient outcomes, and billions of dollars saved in the health-care system. More generally, we anticipate that stretchable, colorimetric fiber sensors may find application in other biomedical devices,[25] athletic wear,[26] and other applications that require color-changing, mechano-responsive textiles.

Experimental Section

Fiber Manufacture: To create multilayer-clad fibers, the precursor for the fiber cladding was first formed, a bilayer of PDMS (Sylgard 184, Dow Corning) and PSPI (432407, Aldrich). These materials were deposited by spin-coating on top of a water-soluble sacrificial layer of poly(4-styrenesulfonic acid) ("PSS," 561223, Aldrich) on a silicon wafer (Figure 2a, top). In parallel, core filaments were fabricated from another variant of PDMS (SE 1700, Dow Corning) to form the cylindrical substrate for the multilayer cladding. This was done by extruding the SE1700 onto a hot plate to facilitate rapid curing and retention of the extruded shape (Figure 2b, top). The dye used to render the cores absorbing prior to extrusion is Silc Pig silicone pigment, supplied by Smooth-On. Once all spin coating steps were complete, the wafer containing the PDMS-PSPI bilayer was slowly immersed in a water bath; the PSS film was thus dissolved, leaving the desired bilayer suspended on top of the water surface, where it could be collected and rolled around an elastomeric core filament (Figure 2c), resulting in the desired cylindrical multilayer structure.

Cyclic Fiber Stretching: The fiber stretching apparatus (Figure S1, Supporting Information) consists of a Thorlabs MTS50-Z8 motorized translation stage used for applying a controlled strain to the fibers, an LCM Systems UF1 force sensor for detecting the corresponding forces to be converted into stresses, and a Prior H101A motorized XY microscope stage to control the position of the stretching motor and load cell with respect to a custom-assembled microscope. The microscope has one optical fiber input for illumination (a Thorlabs SLS201 stabilized broadband light source was used in our experiments), one optical fiber output to an Ocean Optics Maya2000 Pro spectrometer, and a Tucsen IS300 camera in its image plane. Necessary manual adjustment stages were included to allow for the alignment of the fiber samples parallel to the direction of travel of the stage used to create a controlled strain, and to center points of interest in the microscope's focal plane. Control and automation of the stretching motor and positioning stage, and readout of the strain level, force values, and reflection spectra of fibers, were done with WaveMetrics Igor Pro software. Cyclic deformation of fiber samples was done by repeatedly instructing the stretching motor to take specimens to a prescribed level of strain, and then return to a zero-strain state. During analyzed cycles (1, 10, 100, 1000, 10 000), instead of traveling from minimum to maximum strain in one step, strain was applied in 0.05 increments, and stretching was paused at each step. During this pause, the microscope stage moved the fiber to ensure the same point of interest along its length was in the focus of the microscope at each strain, and force data and reflection spectra were recorded. This experiment was carried out with 12 different fibers. All components of a representative data set are shown in Figure 3. For determination of variation in reflected colors along fiber samples, specimens were stretched through a single analysis cycle as described above, with one exception. Instead of tracking the position of a single point on the fiber, the positions of 15–24 points (spaced ≈1 mm apart at zero strain) were tracked, and moved into the focus of the microscope at each level of strain, so reflection spectra could be recorded. This experiment was carried out on 11 fibers. Two representative data sets are shown and discussed in Figure 4c,d.

Pressure–Strain Measurements: Pressure measurement was accomplished with a device modeled after the Kikuhime device,[13]

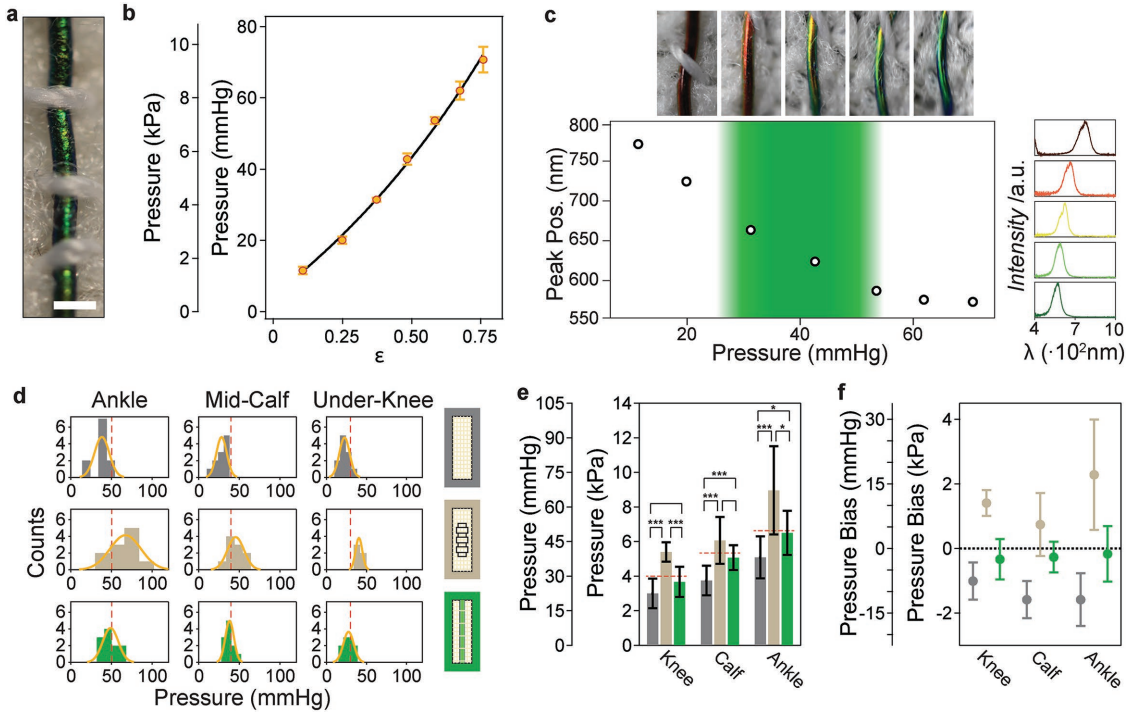

Figure 5. Colorimetric sensing of bandage pressure. a) Fiber stitched onto a bandage. Scale bar 1 mm. b) Bandage pressure versus true strain. Mean and standard deviation are plotted, calculated from $n = 4$ data sets. The black curve indicates a direct proportionality between pressure and engineering strain, indicating that the bandage is deformed entirely within its elastic regime (details are provided in the Supporting Information). c) Peak wavelengths of a fiber for varying applied sub-bandage pressure, which is controlled by adjusting the strain applied to the bandage while wrapping. Images of a fiber integrated in a tested bandage (shown above the plot) were acquired in conjunction with the spectra (shown on the right) at the corresponding pressures. d) Histograms from, and normal distribution fits to, data from volunteers applying unmarked bandages, bandages with geometric strain indicators, and bandages with integrated elastomeric photonic fibers to other volunteers' legs. The yellow curves indicate normal distribution fits to the data. Red dashed lines mark the target pressures. e) Data from (d), plotted as means (bars) with standard deviations (error bars). There were $n = 10$ data points for the geometric bandage at the mid-calf and knee, and for the fiber bandage at the knee. The remaining six data sets contained $n = 11$ points. Red dashed lines indicate target pressures. Brackets between data sets indicate confidence levels with which experimental means are statistically significant, by the two-tailed Welch's *t*-test (***$p < 0.001$, *$p < 0.05$, [no symbol] $p < 0.10$; further details can be found in the Experimental Section). f) Means and estimated bias in each bandage system, with error bars indicating 95% confidence bounds, at each experimental bandage location. Only the bandage with an integrated elastomer photonic fiber had bias that could not be significantly distinguished from zero for all target pressures.

consisting of a small polyurethane bladder connected to a silicone tube attached to a pressure transducer (Figure S2, Supporting Information). To confirm the relationship between strain in an elastic material and the pressure it applied to an underlying substrate, the device was affixed to a leg-simulating pool noodle, which was situated within a rack-and-pinion device that allowed for the application of a constant level of strain to bandages wrapped around the noodle. Opposite ends of a bandage were affixed to the modified pool noodle and an adjustable crossbar. The position of the crossbar, and initial position of the pool noodle, defined the strain in the unwrapped bandage. Pinions at each end of the axle that ran through the center of the pool noodle and racks that ran along the length of the device allowed the bandage to be wrapped around the pool noodle, while maintaining the initial level of strain. Mounts were installed on the frame of the apparatus to allow for either the placement of a digital camera or an optical fiber leading to a spectrometer. (Both were mounted to demonstrate their positions in Figure S2 of the Supporting Information.) Four different fiber-integrated bandages were tested in this manner. A representative data set is shown in Figure 5c.

Fiber-Integrated Bandages: A prototype bandage was made by stitching an elastomeric photonic fiber onto an elastic bandage (ConvaTec SurePress High Compression Bandage). Stitches firmly hold the fiber in place, while allowing it to stretch freely between anchored points. A stitch spacing of 1–2 mm was found to be sufficient for a sure grip, while spacious enough to not significantly affect visibility of the fiber color (Figure 5a). Volunteers were asked to apply the prototype bandage, an elastic bandage with geometric markings to indicate one level of strain, and a plain elastic bandage to other volunteers' legs at three different locations. Regardless of the bandage being used, the volunteers were given targets of 50 mmHg (6.67 kPa) at the ankle, 40 mmHg (5.33 kPa) at the mid-calf, and 30 mmHg (4.00 kPa) just below the knee. If applying a plain bandage, volunteers were given three segments of bandages mechanically limited (Figure S4a, Supporting Information) to achieve the strains necessary to apply these pressures, which can be used to get a feel for how taut the bandage should be to hit the target pressure at each point. For bandages with geometric markings, volunteers were informed that the rectangles on the bandage become squares when a pressure of 40 mmHg is applied. For the bandage with an integrated fiber, the color–strain relation of the fiber was known, and so a chart was produced for the volunteers that depicts the color that is reflected by the fiber at various pressures (Figure S4b, Supporting Information). Volunteers were provided with minimal instruction as to how to apply compression bandages, and were not told what pressures they apply during or between trials. Pressure was measured using the custom-made bladder device described above.

Modeling of Colorimetric Response: A computational multilayer modeling environment was implemented in MATLAB to simulate the reflection spectra of an elastomeric multilayer structure at arbitrary strains, based on the refractive indices and initial thicknesses of the thin films in the multilayer. The model can also account for one or two regions of periodicity in the multilayer, as regions of different periodicity

could be simply obtained by rolling a bilayer up from an axis displaced from both the bilayer's center and its end. This model can be used to predict the resulting color path of a manufactured bilayer before rolling (Figure S5, Supporting Information), and to iterate through numerous initial fiber structures to identify fiber design with desired color paths (Figure 4).

Graphics Generation: The rendering of the bandaged leg in Figure 1a was done using Blender—a free, open source 3D graphics environment. The graphic was composed using a bare leg model created by id4Kohpe on Blend Swap, sourced under a creative commons license. The images in Figure 2a–d are also rendered in Blender.

Statistical Analysis: Meanings of error bars in, and sample sizes of, plotted data vary depending on the data represented and are indicated in the caption of each figure. All spectra shown are representative samples, normalized to the reflection of light off a flat mirror (i.e., a reflection of 0.8 indicates the reflection of 80% as much light at a particular wavelength as a mirror). In determining the significance of differences between mean applied pressures by different bandage systems at similar target pressures, a two-tailed Welch's *t*-test was used. This variant of the *t*-test was optimized for cases where two means have unequal variance, which was hypothesized, and unequal sample size, which was present in the data. In this test, *t*-values were calculated by comparing the sample mean $\bar{X}$, number of points n, and sample variance s^2 of two data sets by

$$t = \frac{\bar{X}_1 - \bar{X}_2}{\sqrt{\frac{s_1^2}{n_1} - \frac{s_2^2}{n_2}}} \tag{2}$$

Factoring in sample degrees of freedom ν (equivalent to one fewer than n), the degrees of freedom associated with the test can be estimated by the Welch–Satterthwaite equation

$$\nu \approx \frac{\left(\frac{s_1^2}{n_1} + \frac{s_2^2}{n_2}\right)^2}{\left(\frac{s_1^2}{n_1}\right)^2 \frac{1}{\nu_1} + \left(\frac{s_2^2}{n_2}\right)^2 \frac{1}{\nu_2}} \tag{3}$$

Bias was calculated by subtracting sample means $\bar{X}$ from target values R. Confidence limits for bias were obtained by multiplying the standard deviation of the mean by the appropriate *t*-value for each data set

$$\left(\bar{X} - R\right) - \frac{\sigma}{\sqrt{n}} t(\nu, P) < B < \left(\bar{X} - R\right) + \frac{\sigma}{\sqrt{n}} t(\nu, P) \tag{4}$$

Values of t, ν, and p can be found in Table S5 of the Supporting Information. Significance level between groups is represented as [no symbol] $p < 0.10$, $*p < 0.05$, $***p < 0.001$. Calculations related to Welch's *t*-test and bias were carried out using these equations in Microsoft Excel. Wavemetrics Igor was used to calculate and plot statistical values for data represented in Figures 2,3, and 5b,c, and e,f. MATLAB was used to calculate areas of standard deviation in Figure 4c,d, and to plot histograms and normal distribution fits (using the "histfit" command) in Figure 5d.

Supporting Information

Supporting Information is available from the Wiley Online Library or from the author.

Acknowledgements

The authors thank Amelia Bryan, Marcus Urann, and Joseph Lowman for support with the manufacture of elastomeric photonic fibers. J.D.S., J.A.L., and M.K. acknowledge support by the National Science Foundation through the "Designing Materials to Revolutionize and Engineer our Future" program (DMREF-1533985). J.A.L. gratefully acknowledges the generous support for this research provided by the GETTYLAB. M.K. thanks the MIT Department of Mechanical Engineering for support.

Conflict of Interest

The authors declare no conflict of interest.

Keywords

biomedical sensing, colorimetric pressure sensing, compression bandages, dynamic photonic materials, tunable photonic fibers

Received: March 21, 2018
Revised: April 19, 2018
Published online:

[1] J. Kaufmann, *Text. World* **2016**, *166*, 36.
[2] J. L. Ng, C. E. Collins, M. L. Knothe Tate, *Acta Biomater.* **2017**, *56*, 14.
[3] A.-A. Ramelet, *Dermatol. Surg.* **2002**, *28*, 6.
[4] K. Zarchi, G. B. E. Jemec, *JAMA Dermatol.* **2014**, *150*, 730.
[5] C. Moffatt, *Int. Wound J.* **2008**, *5*, 259.
[6] G. Mosti, *Phlebology* **2012**, *27*, 1.
[7] K. Keller, G. Krenzer-Scheidemantel, T. Meyer, *Zentralblatt Für Chir.—Z. Für Allg. Visz. Thorax - Gefäßchirurgie* **2014**, *139*, 638.
[8] S. O'Meara, N. Cullum, E. A. Nelson, J. C. Dumville, *Cochrane Database Syst. Rev.* **2012**, *11*, CD000265.
[9] C. K. Sen, G. M. Gordillo, S. Roy, R. Kirsner, L. Lambert, T. K. Hunt, F. Gottrup, G. C. Gurtner, M. T. Longaker, *Wound Repair Regen.* **2009**, *17*, 763.
[10] A. Y. Mousa, B. K. Richmond, A. F. AbuRahma, *Vasc. Endovasc. Surg.* **2014**, *48*, 93.
[11] H. Partsch, *Phlebology* **2014**, *29*, 140.
[12] H. Partsch, G. Mosti, *Int. Angiol.* **2010**, *29*, 426.
[13] N. Brophy-Williams, M. W. Driller, S. L. Halson, J. W. Fell, C. M. Shing, *Sports Eng.* **2014**, *17*, 55.
[14] M. Kolle, A. Lethbridge, M. Kreysing, J. J. Baumberg, J. Aizenberg, P. Vukusic, *Adv. Mater.* **2013**, *25*, 2239.
[15] The Dow Chemical Company, DOWSIL SE 1700, Form No. 11-1785-01 A, https://consumer.dow.com/en-us/document-viewer.html?randomVar=10367486680151645 95&docPath=/content/dam/dcc/documents/en-us/productdatasheet/11/11-17/11-1785-dowsil-se-1700-adhesive.pdf (accessed: October 2017).
[16] V. G. Gupte, in *Color Measurement: Principles, Advances and Industrial Applications* (Ed: M. L. Gulrajani), Woodhead Publishing, Cambridge, UK - Philadelphia, US - New Dehli, India **2010**, Ch. 3.
[17] C. I. Aguirre, E. Reguera, A. Stein, *Adv. Funct. Mater.* **2010**, *20*, 2565.
[18] R. V. Nair, R. Vijaya, *Prog. Quantum Electron.* **2010**, *34*, 89.
[19] M. B. Applegate, M. A. Brenckle, B. Marelli, H. Tao, D. L. Kaplan, F. G. Omenetto, *Opt. Photonics News* **2014**, *25*, 28.
[20] Y. Zhao, Y. Ying, Q. Wang, *Opt. Laser Technol.* **2014**, *64*, 278.
[21] Y. Yue, J. P. Gong, *J. Photochem. Photobiol., C* **2015**, *23*, 45.
[22] G. Kamita, B. Frka-Petesic, A. Allard, M. Dargaud, K. King, A. G. Dumanli, S. Vignolini, *Adv. Opt. Mater.* **2016**, *4*, 1950.
[23] A. Piriya V. S, P. Joseph, K. Daniel S. C. G., S. Lakshmanan, T. Kinoshita, S. Muthusamy, *Mater. Sci. Eng. C* **2017**, *78*, 1231.
[24] A. J. Elliot, *Front. Psychol.* **2015**, *6*, 368.
[25] Q. Chen, S. Liang, G. A. Thouas, *Prog. Polym. Sci.* **2013**, *38*, 584.
[26] L. Zhang, *Adv. Mater. Res.* **2014**, *978*, 31.

